Joachim Klinner
First *Last*

ASME Paper Title: The Unsteady Shock-Boundary Layer Interaction in a Compressor Cascade – Part 1: Measurements With Time-Resolved PIV

ASME Journal Title: ASME Journal of Turbomachinery

Volume/Issue ____147(9)______________________ Date of Publication (VOR* Online) Dec 2024 _________

ASME Digital Collection URL: https://asmedigitalcollection.asme.org/turbomachinery/article/147/9/091001/121083 Shock-Boundary-Layer-Interaction-in-a

DOI: https://doi.org/10.1115/1.4067467

Journal of Turbomachinery. Received September 18, 2024;
Accepted manuscript posted December 17, 2024. doi:10.1115/1.4067467

The Unsteady Shock-Boundary Layer Interaction in a Compressor Cascade – Part 1: Measurements With Time-Resolved PIV

Joachim Klinner [1]
Institute of Propulsion Technology
German Aerospace Center (DLR)
Linder Höhe, 51147 Köln
email: joachim.klinner@dlr.de

Edwin J. Munoz Lopez
Institute of Propulsion Technology
German Aerospace Center (DLR)
Linder Höhe, 51147 Köln
email: Edwin.MunozLopez@dlr.de

Alexander Hergt
Institute of Propulsion Technology
German Aerospace Center (DLR)
Linder Höhe, 51147 Köln
email: Alexander.Hergt@dlr.de

Christian E. Willert
Institute of Propulsion Technology
German Aerospace Center (DLR)
Linder Höhe, 51147 Köln
email: chris.willert@dlr.de

In the first part of this 3-paper-series time-resolved PIV (TR-PIV) is performed in the transonic cascade to elucidate the shock-boundary layer interaction process and to provide comparative data for numerical studies and analysis in part 2 and 3. The application of modern high-speed camera technology combined with a dual-pulse high-speed laser system enabled TR-PIV in the cascade for image areas covering $\sim 30\%$ *of the chord and* $\sim 6\%$ *of the blade pitch at sampling intervals of* 0.18 *convective time units (CTU) for the acquisition of multiple time sequences with duration of* ~ 2000 *CTUs. The sampling rate is sufficient to resolve fluctuations of the separating region and accompanying movements of the shock system. To enable correlations between density variations of the shock system and velocity data, shadowgraphs are acquired synchronously with TR-PIV recordings at the same sampling rate. The TR-PIV and shadowgraph measurement setups, the image processing and the resulting spatial resolutions are described in this part. An analysis of power spectral densities along near-wall rows in PIV data reveals the chord-wise spatial distribution of specific peaks and bands, which are also visible in the shock buffet spectrum. A spectral proper orthogonal decomposition (SPOD) of TR-PIV data is conducted to enable inspection of spatio-temporal modes of velocity fluctuations at specific broad peaks and tones in the buffet frequency range. Results indicate, that upstream of the main shock oblique shock waves occur at higher order harmonics of the fundamental buffet frequency and at specific high-frequency tones. The upstream propagation of disturbances beyond the excursion range of the main shock is demonstrated for the dominant buffet frequency as well as for the high-frequency tone and its first harmonic using cross-correlation maps. To locate possible sources of distinct tones at the entrance of the center passage, a SPOD of high-speed schlieren recordings is performed, capturing the shock systems in three passages. The results show that with these high-frequency tones opposing vibrations of bow and lip shocks occur for neighboring blades.*

Keywords: shock boundary layer interaction, SBLI, transonic flow, high speed PIV, high speed schlieren, experimental, SPOD

1 Introduction

In the design process of transonic turbomachinery blading, the correct prediction of shock instabilities in terms of strength and position is of great importance in order to properly localize separations, which in turn affect both flow guiding and viscous losses, and thus the working range. Furthermore, it is clear that underestimation of the corresponding dynamic pressure loads and inaccurate prediction of the frequency range can have serious consequences for the structural life of the blading. In addition to mechanisms that can govern shock oscillations on a single airfoil, i.e. wave propagation feedback mechanism as described by Lee [1] and global aerodynamic mode instability as described by Crouch et al. [2], additional interactions occur between the blade passages, for example due to oscillating bow shocks emanating from the leading edges of the adjacent blade passage and thus influencing the inflow incidence on downstream passages. Furthermore, small fluctuations in mass flows between the blade passages can lead to additional interactions as opposing shock movements.

For turbomachinery in particular, there is therefore a great need for spatially and temporally well resolved experimental data to provide deeper insight and help identify the mechanisms that lead to self-sustaining shock oscillations.

In the framework of the TEAMAero research project sources of unsteadiness of the SBLI in a non-proprietary transonic cascade TCTA are investigated. The TCTA is operated in the transonic cascade wind tunnel of the DLR Institute of Propulsion Technology. In the present paper of this series we report on TR-PIV performed in a center passage of the cascade which enables inspection of the BL state upstream of the shock boundary layer interaction (SBLI) as well as spectral and coherence analysis of the SBLI in different regions on suction and pressure side. Both the measurement setup and the TR-PIV data base are introduced which provides comparative data for numerical simulations and for deeper data analysis as presented in part 2 and 3 of this series. Time-resolved velocity data and visualizations of density fluctuations are analyzed with respect to characteristic frequencies in their PSD using TR-PIV and TR-Shadowgraphs with shock tracking.

A proper orthogonal decomposition (POD) of spatially high-resolution snapshot PIV data of the TCTA covering an area of shock foot and separation bubble was already published in [3]. It was found that the first spatial POD mode represents velocities in the separation bubble that fluctuate together towards lower or higher velocities, indicating that this mode represents states in

[1] Corresponding Author.
Version 1.18, December 12, 2024

Journal of Turbomachinery. Received September 18, 2024;
Accepted manuscript posted December 17, 2024. doi:10.1115/1.4067467

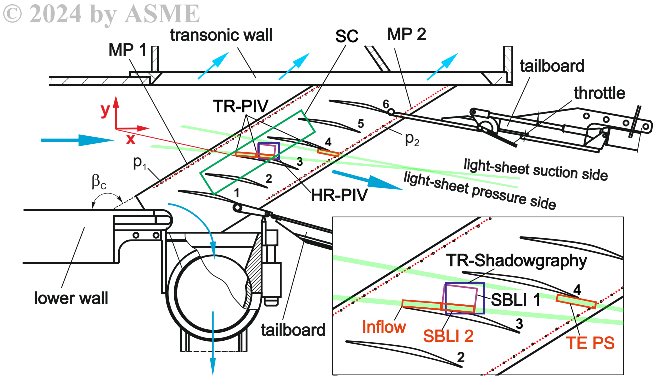

Fig. 1 Test section of the cascade windtunnel and measurement stations for PIV and Shadowgraphy.

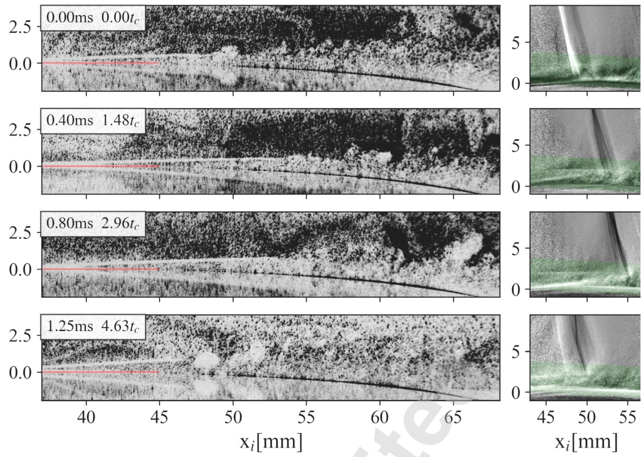

Fig. 2 TR-PIV image sequence in region *SBLI 2* (left) and synchronized shadowgraphs (right), the red line indicates the blade surface, the green region indicates the light-sheet position (color version online).

which the separation zone is either very large or almost non-existent ("breathing mode"). The second POD mode shows an opposite correlation between the velocity fluctuations of the main shock and in the separation region. At higher POD modes, the coherent structures in the separation region tend to be smaller and the spatial modes are divided into smaller structures. In the present contribution these findings are supplemented by a spectral POD (SPOD) of TR-PIV data and high-speed schlieren (HSS) recordings which enables inspection of spatio-temporal modes of velocity and density fluctuations at specific broad peaks and tones in the buffet frequency range. The SPOD allows coherent structures at individual frequencies to be visualized and ranked according to their energy content [4,5].

2 Cascade geometry and operation

The compressor cascade geometry, an experimental validation of the working range and of losses are described in [6], so that only a brief description of the cascade geometry will be be given here. The compressor blade cascade consists of 6 blades with a chord length of $c = 100$ mm, a pitch of 65 mm and a span of 168 mm. Its non-proprietary geometry is representative of a transonic section from a modern compressor rotor. The in-house design process and CFD-based optimization was aimed at minimizing the losses at the design point and over the working range while maintaining representative aerodynamic blade loadings [7]. The cascade is operated in the transonic cascade wind tunnel of the DLR Institute of Technology. At the aerodynamic design point (ADP) investigated here, the chord based Reynolds numbers is 1.3×10^6 corresponding to a inlet Mach number of 1.22. Inlet conditions such as Mach number, static temperature and speed of sound are derived from static pressure measurements at the tunnel sidewalls at the entrance plane MP1 (see Fig. 1) by assuming adiabatic flow and using isentropic gas equations. During testing, the operating parameters of the wind tunnel are adjusted to reproduce a specific isentropic Mach number distribution obtained from chord-wise rows of static pressure tapping points at mid-span on the suction side of blade no.3 and on the pressure side of blade no.2.

3 Experimental methods

3.1 Image acquisition setup. Recording PIV samples with both high spatial and temporal resolutions in compressor cascade flows under relevant operating conditions reaches the limits of current camera technology, which allows frame rates of maximum 30 – 50 kHz with image sizes of 1 MPixel while state-of-the art double frame cameras for PIV enable image sizes up to 5 MPixel at double frame rates of 25 Hz. At the same time, tracking the fastest structures in transonic flows with adequate spatial resolution at velocities exceeding 400 m/s would require frame rates in the megahertz range. For this reason, two different camera configurations were applied in successive measurement campaigns. After commissioning of the cascade conventional PIV measurements recorded at 25 Hz sampling provided an overview of the flow field by capturing particle images in a relatively large field of view in the center passage [3]. Of these earlier PIV setups, imaging and evaluation parameters for the high-resolution configuration (HR-PIV) covering BL lift-off, SBLI and separation are also provided in Table 1. For TR-PIV, a second imaging system was set up for capturing particle images in three specific narrow image regions at high temporal resolution (cf. Fig. 1). An in-house designed double-pulse high speed laser system is used, which can provide small pulse separations in the order of 1 µs at repetition rates exceeding $f_s = 20$ kHz. Previous studies on the TCTA with high speed schlieren (HSS) have shown that the frequency band of fluctuations of the near normal shock position ends below 10 kHz [8]. Therefore, the image acquisition rate for TR-PIV was set between 40 – 46 kHz corresponding to a PIV sampling frequency of 20 – 23 kHz or time intervals of $0.16 - 0.19\, t_c$. The laser light sheet is placed at mid-span through a rigid, air-purged light-sheet probe that is positioned about $4\,c$ downstream of the TE of blade no. 4. With the laser system providing 2×10 W on average, sufficient particle image intensities can be achieved at a light sheet height of 4 mm and 0.2 mm thickness.

Dense smoke oil-based seeding provided by a smoke generator (Vicount) is injected into the settling chamber upstream of the test section. A centrifugal pump facilitates aerosol sizes < 1 µm.

TR-PIV recordings were acquired with a high-speed camera (Phantom v2640, Vision research) equipped with a macro lens (Nikon, Nikkor Micro f200/4) at a magnification of 19.6 µm pixel^{-1}. The high-speed camera was operated with a reduced image size between 1792×200 pixel (46 kHz) and 1792×328 pixel (40 kHz). Frame straddling was applied, and the PIV sampling rate corresponds to half the frame rate. The three regions in which TR-PIV was performed are indicated in Fig. 1, for which imaging parameters are summarized in Table 1. To improve statistical convergence, 8 bursts were recorded at each station at 0.25 Hz repetition, with each burst is containing 10 561 – 12 347 double images corresponding to a duration between 0.52 – 0.53 s ($\approx 2000\, t_c$).

Figure 2, left shows sample particle images obtained with TR-PIV in region *SBLI 2*. In these particle images, a lack of tracer particles in the laminar BL due to inertia selection on the LE is evident, as also observed in previous PIV experiments on shock-laminar BL interactions [9,10]. By mixing in the particle-laden air these particle images provide visualization of both the lift-off of BL and the unsteady laminar-turbulent transition moving down- and upstream with the passage-shock as shown in the shadowgraphs.

Journal of Turbomachinery. Received September 18, 2024;
Accepted manuscript posted December 17, 2024. doi:10.1115/1.4067467

Table 1 Schlieren (Sc), shadowgraph (Sh) and PIV imaging and evaluation parameters, PIV cross-correlation accuracy (Corr. acc.) is provided for 0.1 pixel random peak detection accuracy.

Exp.	Region	f_s [kHz]	Samples [$x10^3$]	Δt [µs]	FOV PIV [mm^2]	m PIV [µm/pixel]	Size IRW [mm^2]	Corr. acc. [m/s]	FOV SH/SC [mm^2]	m SH/SC [µm/pixel]
HR-PIV	SBLI 1	0.025	15.0	0.5	33×28	13.0	0.31×0.31	2.17	-	-
TR-PIV	Inflow	21	8×11.1	1.5	35×6.1	19.5	1.25×0.62	1.30	14.2×14.2	27.9
							1.25×0.12			
TR-PIV	SBLI 2	20	8×10.6	1.0	35×6.4	19.6	1.25×0.63	1.96	23.0×25.5	45.7
							1.25×0.31			
							1.25×0.12			
TR-PIV	TE PS	23	8×12.3	2.0	35×3.9	19.7	0.47×0.47	0.98	13.7×13.7	27.7
TR-SC	SC	20	2×9.64	-	-	-	-	-	205×51.2	100

To assess global shock vibrations of the upstream bow and lip shocks in addition to the main shock in passage 3-4, HSS recordings were also analyzed, which record fluctuating density gradients in region *SC* between blades 2-5 at 20 kHz (cf. region *SC* in Fig. 1). The schlieren image data was recorded within an z-type schlieren setup at a frame rate of 20kHz [8]. Sample HSS sequences at the ADP are shown in [11].

Due to shading of the z-path for schlieren imaging with the high-speed PIV camera, schlieren images could not be recorded simultaneously over the three central passages. Instead, in order to align vibrations of the main shock in passage 3-4 with velocity fluctuations recorded in separate regions, shadowgraph imagery is acquired synchronous with TR-PIV recordings using a second high-speed camera (Phantom v1840, Vision research). Equipped with a Nikkor Micro f200/5.6 lens, the camera captures shadowgraphs in a FOV of $23 \times 23\,\mathrm{mm}^2$ (cf. Fig. 1) at an image scale of $45\,\mu\mathrm{m\,pixel}^{-1}$. Although the camera remains more or less at the same position when moving the TR-PIV camera towards other measurement stations, structural limitations (size of both HS-cameras, camera supports, side wall suction ports) require a larger working distance of the camera used for shadowgraphs, which is why the focal length had to be extended with the help of a teleconverter when TR-PIV is recorded at the remaining stations *Inflow* or *TE PS*. Due to the doubled focal length, the FOV then is significantly smaller. However, passage shock oscillations at maximum range (13% of c) can still be recorded. To enable both a large measuring field and a frame rate that equals the half frame rate in TR-PIV, the camera was operated with 2×2 binning. Since both cameras record partially overlapping image areas at *SBLI 2*, the observation paths were separated by a dichroic mirror, so that shadow images had to be recorded in a different spectral range than with PIV (green laser), as described in detail in [10]. For this reason, a high-power LED emitting in the red (Luminus Phlatlight CBT90-RX) was used for the inline illumination of the passage flow which can provide high-power short-duration pulses of an width of 2 µs at the required frame rates [12].

Both cameras were synchronised in terms of their frame rate, with the PIV camera serving as the master and providing an image synchronisation signal for the second camera, which ran at half the frame rate. However, issues with the trigger mechanism prevented the cameras from obtaining the simultaneous images intended. Instead, the recordings lag each other by two seconds and correspond to non-overlapping time windows. Additionally, cross-correlations of the shock movement and velocity gradients from the different recordings help align some sequences of interest for visualization, as it was originally intended and as shown in Fig. 2 and Fig. 14.

3.2 PIV processing. Before the actual PIV evaluation, vibrations of camera and blade surface were compensated. Therefore, using a correlation-based algorithm the relative position of the blade surface was determined for each image in a small rectangular sample region containing the laser flare on the blade suction side at mid-span. To estimate the image shift in each sample, the intensity distribution in each sample region was correlated with several template images of reference blade positions where each template is shifted by a defined amount in the sub-pixel range. The vertical blade displacement at maximum cross-correlation coefficient is then used to offset the image data to a coincident blade position with an accuracy of < 0.2 pixel prior to further PIV processing. The PSD of the wall vibrations in Fig. 3 shows a dominant peak at 400 Hz (Sr= 0.11) at maximum vibration amplitudes of ±150 µm, which corresponds to a natural frequency of the cascade blade, as determined by ping testing.

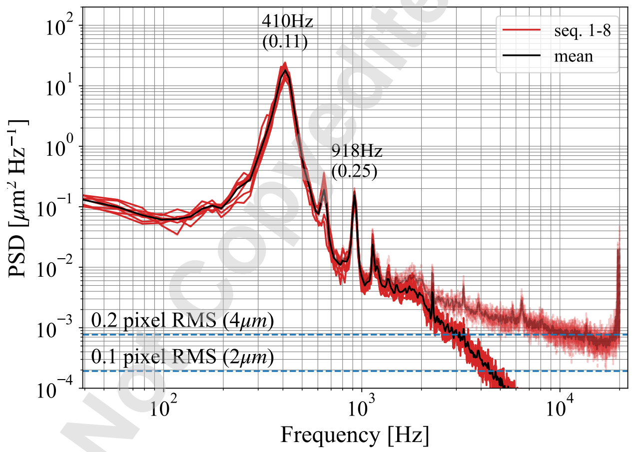

Fig. 3 PSD of blade and camera vibrations at mid-span (Strouhal number provided in brackets), faded lines shows unfiltered data. Vibration data is used to adjust blade position at mid-span to a uniform image position.

To process the HR-PIV recordings, image enhancement is applied to improve particle image contrast which increases the data validation rate in the subsequent cross-correlation analysis. Here, a minimum intensity image calculated from each image sequence is subtracted followed by a clipping of intensities above 98% of the cumulative intensity range. To further enhance particle image contrast and to compensate for intensity variations, images are high pass filtered by a Gaussian kernel of more than twice the width of the largest particle images. Using a standard coarse-to-fine PIV processing algorithm with a final interrogation window size of 24×24 pixel ($0.31 \times 0.31\,\mathrm{mm}^2$ for region *SBLI2*) achieves validation rates of 98%. The corresponding validation scheme is based on normalized median filtering with a threshold of 4.0 [13].

Using a similar PIV processing for TR-PIV, validation rates of at least 97% per burst were feasible using the same validation scheme at a final IRW of 64×32 pixel ($1.25 \times 0.62\,\mathrm{mm}^2$). The corresponding final spatial resolutions in terms of interrogation window sizes are provided in Table 1. If not stated otherwise, the PIV grid resolution is 0.75 of the IRW size. For the modal decomposition (SPOD) of region *SBLI 2* the window size was reduced by a fac-

Journal of Turbomachinery. Received September 18, 2024;
Accepted manuscript posted December 17, 2024. doi:10.1115/1.4067467

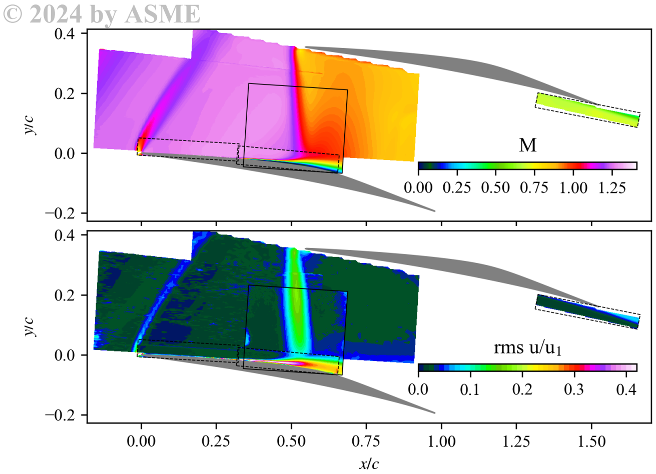

Fig. 4 Mean flow field combined of PIV in six measurement regions between blade no. 3 and 4 at the ADP, solid rectangle: FOV HR-PIV *SBLI 1*, dashed rectangles: FOV TR-PIV (color version online).

tor of two (16 pixel) along image columns to enhance visibility of structures in the separation bubble and to reduce the window overlap with the blade edge. This was accompanied by a reduction in the validation rate to at least 95% per burst. Seamless time traces involve the replacement of outliers based on a spatial median filter that includes the 8 neighboring IRWs. For evaluation of BL thicknesses upstream of the shock-foot, the size of interrogation window in blade-normal direction was further reduced to 6 pixel (120 µm) and a vector spacing of 40 µm in order to minimize overlapping with the blade edge and to achieve high spatial sampling. The cross-correlation accuracy estimates provided in Table 1 are based on a signal peak detection accuracy of 0.1 pixel in the cross-correlation plane during PIV processing. All particle images were evaluated using commercial software (PIVview 3.9) and an in-house Python-based PIV package.

4 Results and Discussion

4.1 Overview of the velocity field in passage 3-4. Fig. 4, top, provides the mean isentropic Mach number at mid-span between two neighbouring blades no. 3 and 4 at ADP and is compiled from velocity magnitudes measured by PIV in six regions of the passage. The Mach number is based on velocity magnitude and the speed of sound at reference plane MP1. The leading edge of the upper blade causes a bow shock which on the pressure side is being intensified and crosses the passage impinging on the suction side of the blade below.

Fig. 4, bottom, exhibits a significant rise of the rms in the axial component within the passage to levels up to 20% which is associated with increased shock vibrations in this area. From shock tracking in up to 15 000 HR-PIV snapshots it could be determined that these high fluctuations are primarily associated to variations of the shock position by up to 13% of chord ($\Delta_{\max} = 0.13\,c$). High turbulence intensity is also generated near the leading edge by vibrations of the bow shock and in the TE wake with levels of approximately 14 and 8%, respectively. Aside from these fluctuations, the highest dynamics are present below the shock foot where the flow separates and a shear layer is being formed.

4.2 Boundary layer condition upstream of the shock foot. The size and shape of the incoming BL upstream of the shock foot was evaluated from several particle image columns indicated in Fig. 5. Velocities were fitted with the Blasius profile in order to determine edge velocities and BL thickness as well as the integral quantities derived from it (cf. Table 2). Since momentum and displacement thicknesses require density weighting in compressible

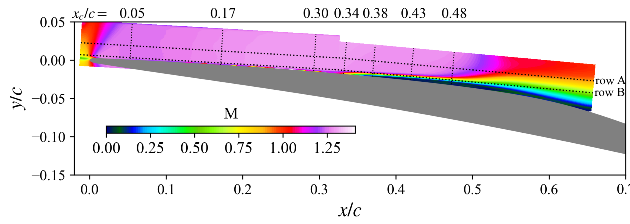

Fig. 5 Mean isentropic Mach contour near the suction side and columns and rows from which velocity profiles were extracted (color version online).

flows, the temperature profiles were estimated based on the edge Mach number assuming constant static pressure in the BL. Therefore, according to [14], a coupling relation between temperature and velocity was applied to estimate temperature profiles (Fig. 6) under the assumption of an adiabatic wall-temperature and a recovery factor of 0.82 (laminar BL overs a flat plate). Mean velocity profiles in Fig. 6 indicate that from $x_c/c = 0.34$ the edge thickness increases significantly, while negative wall-parallel velocities in the near-wall region indicate the BL lifting-off and thus the beginning of separation.

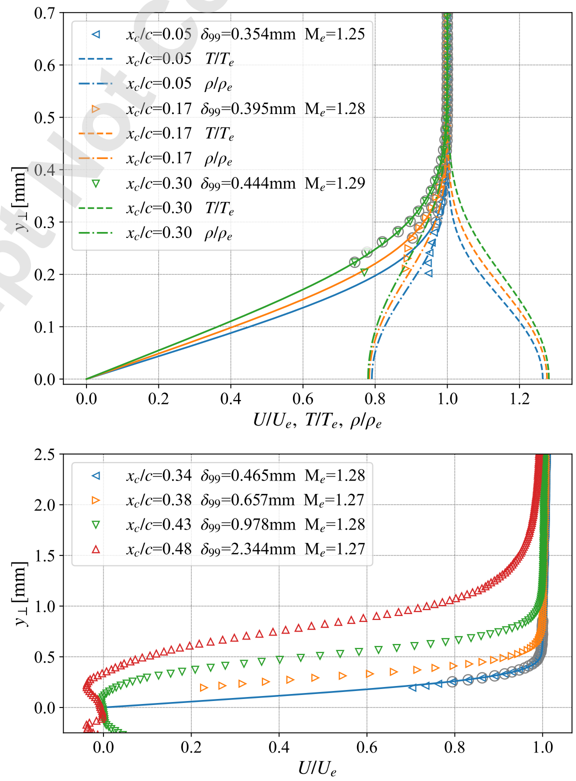

Fig. 6 BL profiles measured with TR-PIV at different image columns as indicated in Fig. 5, solid lines represent the Blasius-fit, circles indicates data points included in the fit.

4.3 Spectral analysis. To evaluate the buffet frequencies of the main passage shock within $0.10 \le y/c \le 0.17$ (cf. Fig. 14, top), in each shadowgraph the local minima of the image row intensities was evaluated and averaged along the corresponding image rows. Using Welch's method, the premultiplied PSD of passage shock vibrations was estimated for each of 8 bursts and then averaged. Figure 7 confirms that the PSDs of the main shock oscillation increase from 0.2 kHz up to a peak near 0.5 kHz, hereinafter referred to as *dominant buffet frequency*, f_b, and then decays to

Journal of Turbomachinery. Received September 18, 2024;
Accepted manuscript posted December 17, 2024. doi:10.1115/1.4067467

Table 2 Estimates of BL parameters obtained from Blasius-fits (cf. Fig. 6) for the ADP; δ_c^* and θ_c include density-weighting according to [14].

x_c/c	δ_{99} [µm]	δ^* [µm]	δ_c^* [µm]	θ [µm]	θ_c [µm]	H_c δ_c^*/θ_c
0.05	354	124	141	48	41	3.42
0.17	395	138	159	53	46	3.46
0.30	444	156	179	60	51	3.47
0.34	465	163	187	63	54	3.46

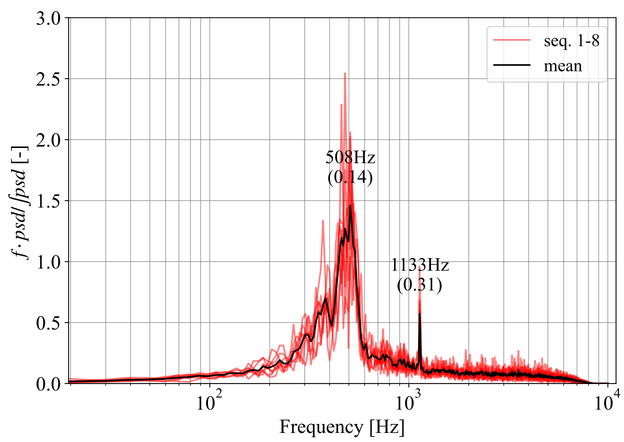

Fig. 7 Premultiplied PSD of vibrations of the main shock in passage 3-4, binwidth Δf=9.8 Hz, Strouhal number in brackets.

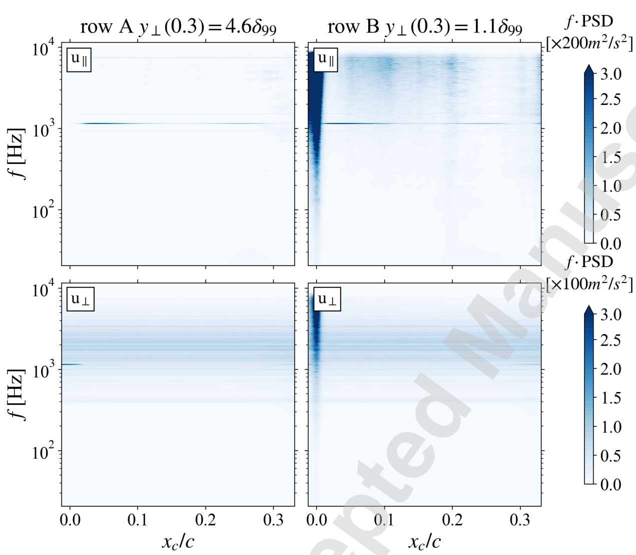

Fig. 8 Premultiplied chordwise PSD of longitudinal and transverse velocity fluctuations in region *inflow Bl*, binwidth Δf = 10.3 Hz (color version online).

0.8 kHz. A similar distribution was already measured by [8] by analyzing high-speed schlieren recordings of the TCTA. The tone at 1.1 kHz is also confirmed, and we will come back to possible origins of this tonal vibration in the discussion of the SPOD analyses.

To further analyze which significant frequencies are transmitted by wall-parallel ($u_\parallel$) and wall-normal ($u_\perp$) velocity fluctuations near the suction side, PSDs of these components were evaluated using Welch's method along two chord-wise particle image rows, which pass one far and near the suction side with wall distances of $4.6\delta_{99}$ and $1.1\delta_{99}$ at $x_c = 0.3c$, respectively (cf. row A and B in Fig. 5).

Figure 8 again shows the pronounced peak at 1.1 kHz in the transverse component upstream of the lip shock for the far-wall row *A*, which indicates that this tone is already transmitted into the passage from upstream of the LE, probably by small phase locked variations of $u_\perp$ that originate from the preceding bow shock, which is discussed in more detail in section 4.5 based on a SPOD of TR schlieren recordings covering 3 passages. If the PSD is followed further along row *A*, it becomes apparent that the flow is redirected via the lip shock, which leads to a PSD drop of the wall-normal component in favor of the wall-parallel component for the tone and thus increases the PSD of $u_\parallel$ at 1.1 kHz (cf. Fig. 8, left) , which then decreases further along the chord. Along row *B* near the wall (cf. Fig. 8, right), strong fluctuations occur upstream of the lip shock ($x_c < 0.02\,c$) and near the LE, which, however, do not coincide with the maximum of low-frequency shock oscillations of the passage shock at $f_b = 0.5$ kHz and clearly decay for $u_\parallel$ approximately up to $x_c = 0.2\,c$. The wall-normal component in row *A* and *B* shows constant broadband fluctuations along x_c with a maximum near 2 kHz. Also, there is a weak tonal oscillation of the $u_\perp$ component at 0.4 kHz, also constant along x_c, which most likely results from the natural frequency of blade oscillation which was confirmed by ping-testing (cf. Fig. 3).

Figure 9 presents a similar evaluation of PSDs in region *SBLI 2* supplemented by PSDs at distinct positions $x_c = 0.36c$ (entry into the separation bubble) as well at two positions immediately upstream and downstream of $\overline{x_s}$.

For the far-wall row *A* (cf. Fig. 9, left), the dominant buffet frequency occurs immediately upstream of $\overline{x_s}$ in the PSD of $u_\parallel$, increases by a factor of about 10 at $x_c = 0.55\,c$ and remains visible above the shear layer (cf. Fig. 5) until it exits the FOV. The fluctuations of transverse components $u_\perp$also show the dominant buffet frequency upstream and downstream of $\overline{x_s}$, but these disappear in the further course of row *A* when entering the shear layer (cf. Fig. 5).

Figure 9 (right) shows that near the wall, where row *B* enters the separation bubble ($x_c = 0.36\,c$), large fluctuations of the wall-parallel component occur at the dominant buffet frequency, probably due to partially shock-synchronous lifting of the laminar BL (cf. Fig. 2). The frequencies of fluctuations partly correspond to the dominant shock oscillation in Fig. 7, but decay in the further course of row *B* up to the main shock. In addition, there are fluctuations in a band above the third harmonic of the main buffet frequency with a maximum at 1.8 kHz. In addition to the tone at 1.1 kHz already visible in PSDs far upstream (cf. Fig. 8), the PSD of the first harmonic of that tone (≈ 2.2 kHz) is significantly larger upstream than downstream of the main shock which has also been confirmed by spectral analyses of shadowgraphs as described in part 3 of this paper session. Inspection of Fig. 9 reveals, that the PSD at the 1st harmonic of the tone is significantly higher at the near-wall line *B* than at the far-wall line *A*, which could indicate that these fluctuations originate from the separation bubble, which was also observed during the inspection of the TR shadowgraphs and will be discussed in one of the following sections 4.6.

4.4 Spectral Proper Orthogonal Decomposition. To determine which spatial structures are assigned to which frequencies at the passage entry and in regions covered by TR-PIV, a spatio-temporal modal decomposition was performed separately for HSS and PIV recordings. In comparison to a POD, the SPOD is conducted in frequency space, whereby an energy ranking is provided [4,5]. Processing was conducted using the package [15].

That the SPOD of HSS is a valid tool for analyzing SBLIs has already been demonstrated in previous work by [16,17]. For the cascade flow, to keep the problem size manageable on a standard workstation with 16-cores and 64 GByte RAM, schlieren images were downsampled by a factor of 2. Instead of decomposing a full 3d array of shape $nt \times ny \times nx$, pixels that cover the blade and

Journal of Turbomachinery. Received September 18, 2024;
Accepted manuscript posted December 17, 2024. doi:10.1115/1.4067467

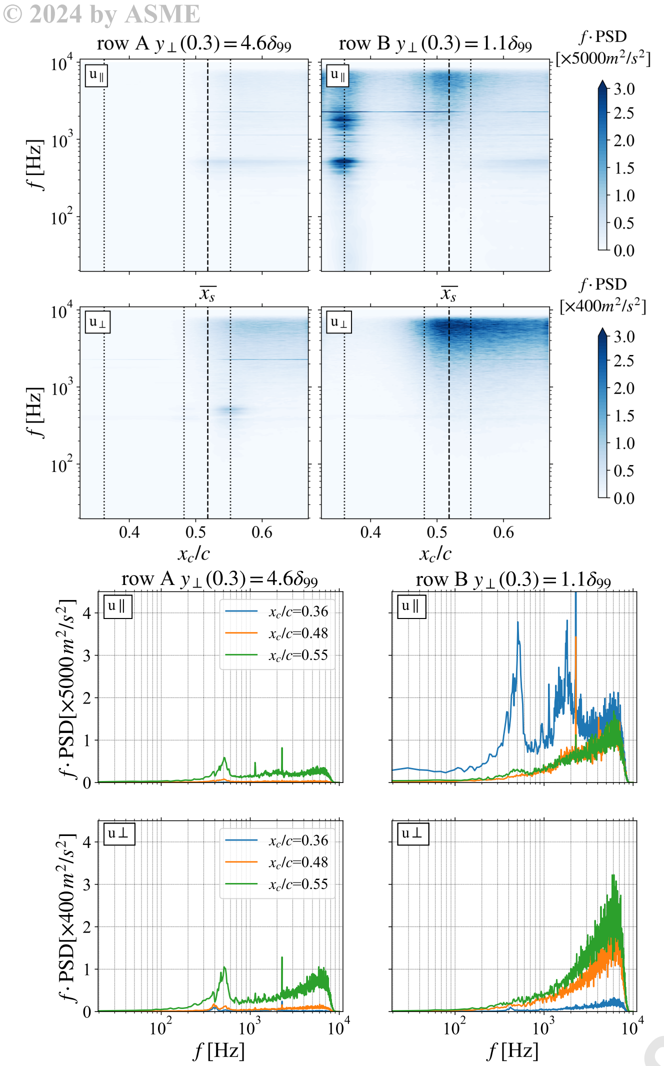

Fig. 9 Top: Premultiplied chord-wise PSD of longitudinal and transverse velocity fluctuations in region *SBLI 2* (color version online), mean position of the passage shock is indicated by the dashed line; Bottom: PSDs at positions marked by red dotted lines.

vibrating pressure hoses where excluded and processing was done on the remaining pixels in form of a 2d array $nt \times n$ pixels. Image preprocessing included centering by the mean of the sequence and dividing by the mean to mitigate inhomogeneities in the backlight. Similarly, processing of u and v components from PIV also involved centering by their mean.

Due to RAM limitations processing of schlieren recordings is done separately on each sequence covering 0.482 s (1785 t_c) which is grouped into $N = 8$ blocks of $N_{\text{FFT}} = 2048$ samples (379 t_c). As a decomposition of PIV datasets with about 8 times less grid points is less memory demanding, the entire TR-PIV dataset of duration 8×0.528 s ($8 \times 1956\, t_c$) is grouped into $N = 79$ blocks the same window size N_{FFT}. To avoid spectral leakage, each block is windowed by the Hamming window function and is overlapped with neighboring blocks by 50%.

A Fourier transform is applied to each block at $f_m = m\, N_{\text{FFT}}\, f_s$ discrete frequencies with a bin size of $\Delta f = f_s / N_{\text{FFT}} = 9.8$ Hz. The remaining processing is done at one frequency f_m at a time. From Fourier transformations per f_m, the sampling matrix $\hat{Q}$ is grouped, which has a size of $N \times M$, where M corresponds to the degree of freedom, which is $2 \times ny \times nx$ involving two velocity components. From $\hat{Q}$ the cross-spectral density is estimated

$$\hat{C} = \frac{1}{N-1} \hat{Q} \hat{Q}^H \qquad (1)$$

Finally the eigenvalue decomposition is performed on the cross-spectral density tensor to obtain the SPOD modes

$$\hat{C} W \hat{\Phi} = \hat{\Phi} \hat{\Lambda} \qquad (2)$$

For TR-schlieren, uniform weighting is applied on the basis of the variance of recorded intensity. For TR-PIV data, the weighting matrix W is based on the 2-norm for the velocity vector $[u, v]$ to provide a partial estimate of the turbulent kinetic energy. As the 8 PIV-bursts per test point are not connected in time at the edges, the merged input data was analyzed with and without overlap. As the shape of examined real parts of the SPOD modes remained similar but weaker without overlap, the entire data set was analyzed with 50% overlap, which also resulted in a smoother SPOD spectrum.

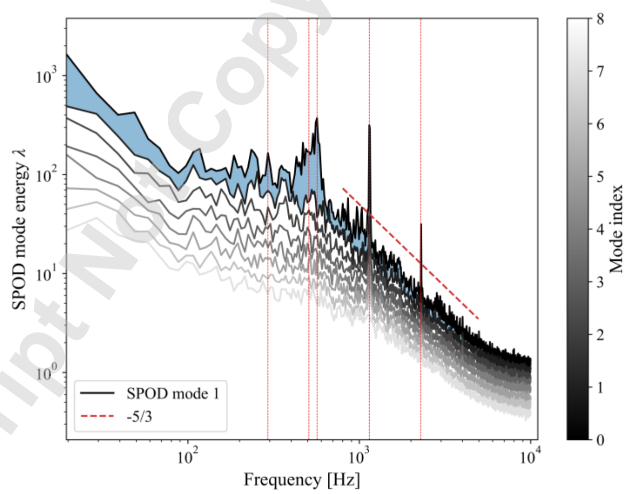

Fig. 10 Mode spectrum from SPOD decomposition of HSS recordings in region *SC* for blocks of $N_{\text{FFT}} = 2048$ samples corresponding to 379 t_c per block.

4.5 SPOD results. The energy spectrum from HSS recordings shown in Fig. 10 features similarities with the spectrum of shock vibrations of the main shock in passage 3-4 in Fig. 7, that are the broad low frequency peak near 0.508 kHz, the tone at 1.1 kHz and its first harmonic. For the schlieren images, additional peaks occur in the low frequency buffet range, for example at 0.293 and 0.566 kHz. For the low frequency peaks a large part of energy is contained in the first mode as indicated by the relatively large area between the curves of the first two modes at these frequencies. Inspection of the shape of the first mode at 0.507 kHz (i.e. dominat buffet frequency in passage 3-4) in Fig. 11 (second plot) reveals that the main shocks in three passages oscillate in-phase , which is also evident from the temporal course of the reconstruction of the first mode [11]. This in-phase movement in neighboring passages is surprising, as it was assumed, that if a higher back pressure is established in one passage, neighboring passages tend to dethrottle, i.e. the shock oscillates in anti-phase. This is the case for anti-phase oscillation observed at 0.293 kHz (leftmost plot) and at 0.566 kHz (third plot) which have a similar or higher eigenvalue (cf. [11]). The third plot in Fig. 11 shows that the local maximum at 0.566 kHz (cf. Fig. 10) can be assigned to an oscillation that is essentially restricted to the passage 2-3 and is probably related to deviations from periodicity, as they inherently occur in linear transonic cascades. Although care was taken in the cascade tests

Journal of Turbomachinery. Received September 18, 2024;
Accepted manuscript posted December 17, 2024. doi:10.1115/1.4067467

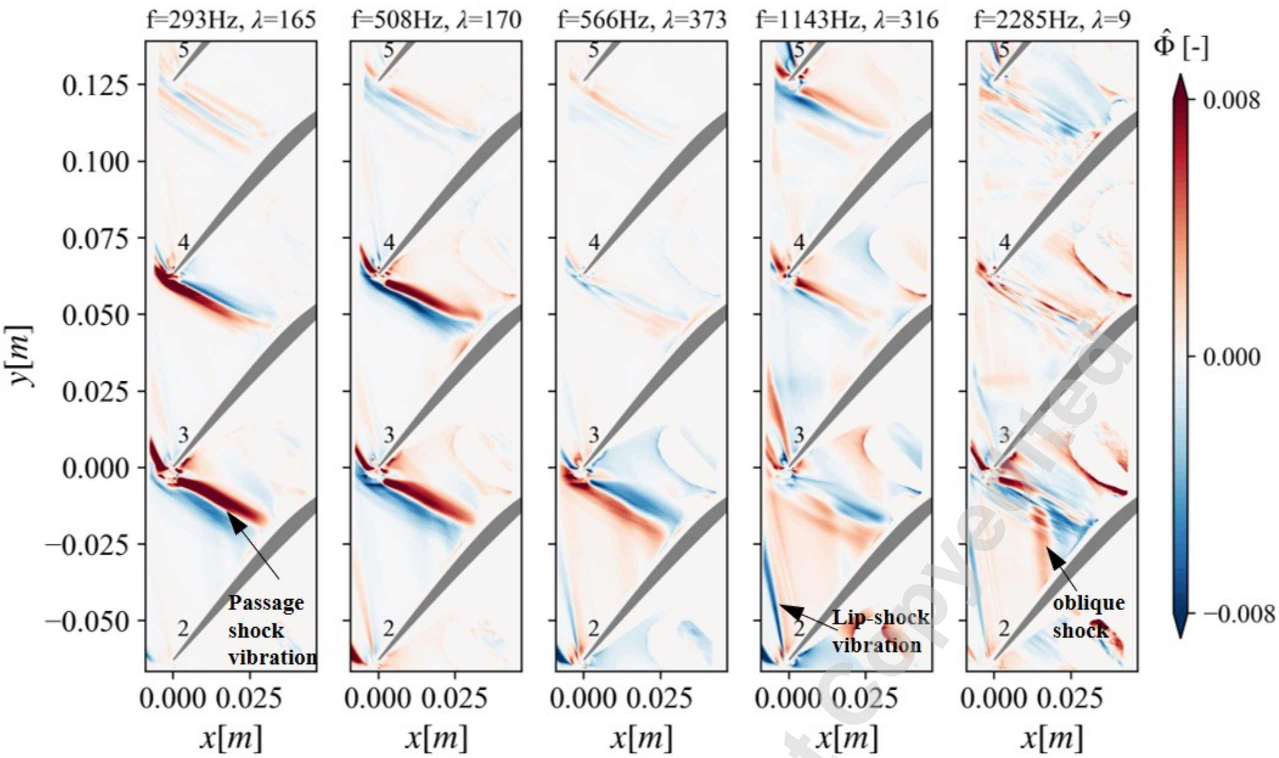

Fig. 11 First SPOD mode from decomposition of HSS recordings at dominant frequencies in region *SC* (color version online); for a temporal reconstruction of the first mode cf. [11].

to set up the middle passage with the most periodic conditions possible, deviations from periodicity for a passage up and downstream are unavoidable as the inflow passes through a different number of bow shocks and shock reflections before entering the passage [6]. This could also explain the decreasing correlation of main shock oscillations for 0.293, 0.508, 0.566 kHz as the blade number increases. Measured deviations of the inflow angel near the bow shocks of blade no.3 and 4 were quantified by L2F measurements in MP1 and amount to a maximum of 0.7% of the nominal inflow angle [6].

We now come back to the dominant tonal peak at 1.1 kHz, which is very pronounced both in the vibrations of the main shock in passage 3-4 and in the PSDs of $u_\perp$ near the leading edge of blade no.3 in Fig. 8. Inspection of the mode reveals, that at this frequency the bow and lip shocks near the LE of blade no.2 and 3 oscillate in anti-phase (cf. [11]). The mode shape indicates that a coherent disturbance spreads upwards over the area between the lip shock of blade no.2 and the bow shock of blade no.3 thereby periodically varying the inflow angel near the LE which demonstrate the transmission of this frequency between neighboring blade passages. The furthest right plot in Fig. 11 shows, although at a very low eigenvalue, that at the first harmonic of the tone oblique shock structures occurs at the foot of the main shock in the lower passage $2-3$, indicating a thickening of the subjacent separation bubble oscillating at this frequency. Such high frequency variations should also occur in spatio-temporal modes of the measured velocities, which will now be discussed.

Figure 12 presents the modal energy spectrum of the first nine modes obtained from decomposition of the CSD of Fourier transforms of velocity within the FOV *SBLI2* in passage 3-4. Most of the energy is contained in the first mode. A large area between the curves of the first two modes indicates a so-called low-rank behavior at certain frequencies or frequency bands, meaning that a large part of mode energy is represented by the first mode. There is broad low-rank peak near the dominant buffet frequency at 0.508 kHz as

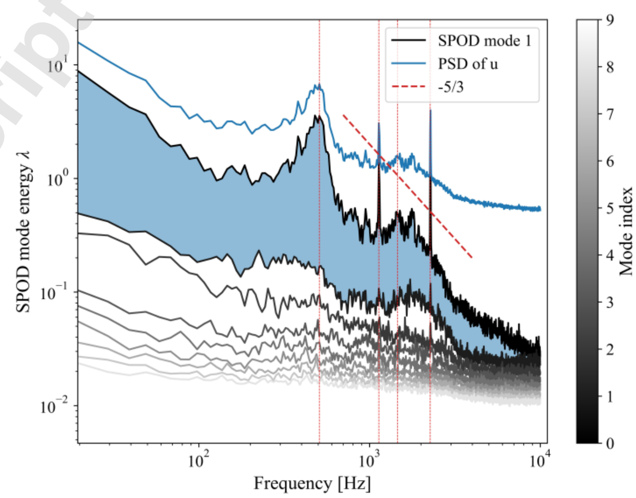

Fig. 12 Mode spectrum from SPOD decomposition of PIV samples in region *SBLI 2* for blocks of N_{FFT} = 2048 samples corresponding to 379 t_c per block.

well as the tonal peaks near 0.113 kHz (also visible in Fig. 7) and its first harmonic at 0.227 kHz. A small peak also occurs near the third harmonic of the main buffet frequency at 0.146 kHz which is not present in mode no.2. Furthermore, from mode no.7 the spectrum exhibits a rather uniform distribution indicating a noise floor, which confirms that the consideration of lower modes (i.e. a low order model) allows an efficient noise suppression in the measurements as well as error estimations (see also [5]). For these relevant frequencies, the SPOD modes for u and v including the modal energy at this frequency λ are shown in Fig. 13. An SPOD evaluation over longer blocks (N_{FFT} = 4096) resulted in similar

Journal of Turbomachinery. Received September 18, 2024;
Accepted manuscript posted December 17, 2024. doi:10.1115/1.4067467

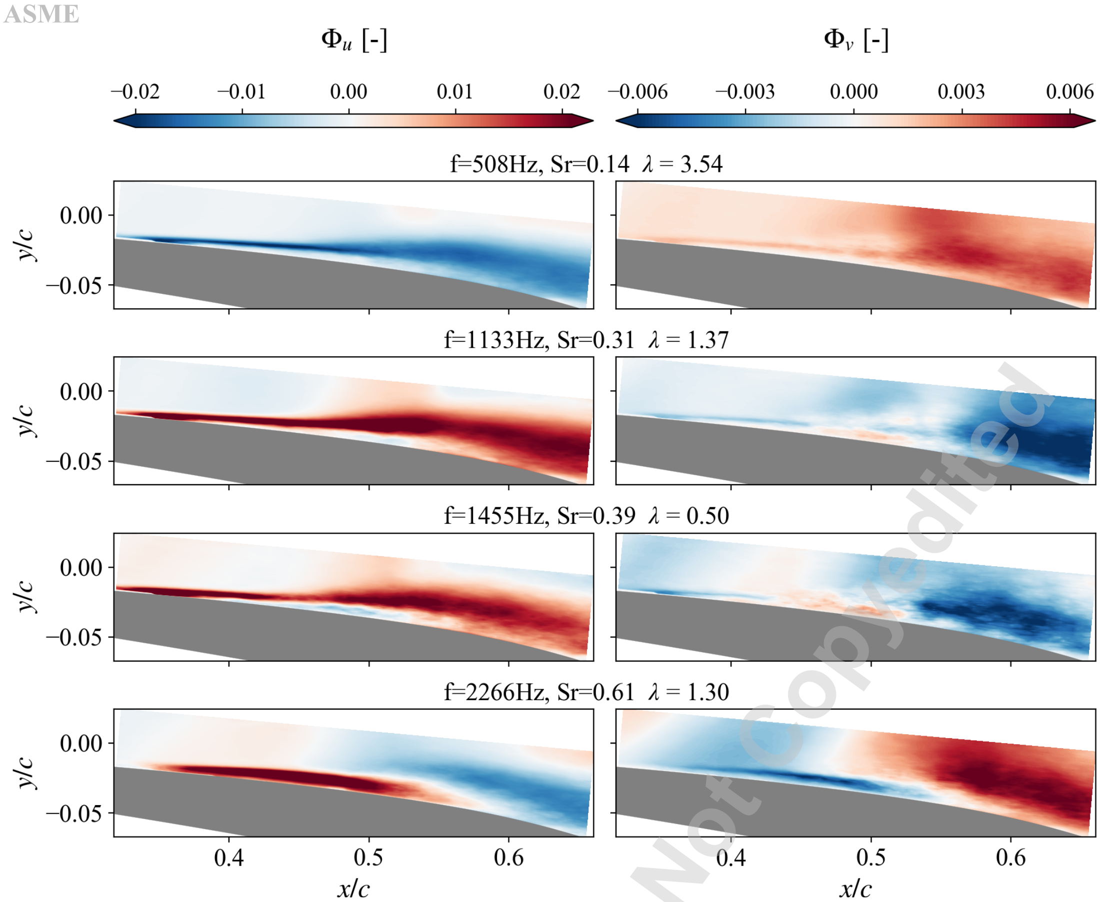

Fig. 13 First SPOD modes for dominant frequencies in velocity fluctuations in region *SBLI 2* (color version online); for the corresponding temporal reconstruction of 2d velocities cf. [11].

mode shapes at relevant frequencies, which is why we consider the flow within block length as statistically stationary.

At the dominant buffet frequency (cf. Fig. 13, top row), uniform velocity fluctuations occur in the separation region which has similarities with POD mode no.1 [3] as it indicates that velocities in the separation region fluctuate together toward lower or higher velocities. This can be interpreted that states at which the separation zone is either very large or almost nonexistent (flow is attached) mainly oscillate with the shock motion at the dominant buffet frequency. This is also evident from the higher coherence between transverse velocity fluctuations downstream of the shock in Φ_v as well as from the temporal course of the reconstruction of 2d velocities at this frequency provided in [11]. At the tone near 1.13 kHz no major differences to the behavior at 0.5 kHz are visible, except for much smaller variation in position of the shock foot (cf. [11]) and the appearance of an isolated zone of a coherent fluid package within the separation bubble in Φ_v. This isolated zone increases when inspecting the mode shape for the second harmonic of f_b near 1.45 kHz (third row). In addition, structures become visible that indicate oblique shock waves in Φ_v. The visibility of oblique shock structures increases significantly in Φ_u and Φ_v for the first harmonic of the tone at 2.27 kHz which has a threefold higher eigenvalue λ in comparison to the fundamental frequency. The high impact on the separation region size is also evident from the reconstruction of 2d velocities at this frequency provided in [11]. These oblique waves occur approximately four times over one buffet cycle. The appearance of the oblique shock is accompanied by larger coherence of Φ_u in the isolated fluid package in the separation bubble at 2.27 kHz.

4.6 Correlations between shock traces and and velocity.

The spatio-temporal modal analysis in the previous sections showed

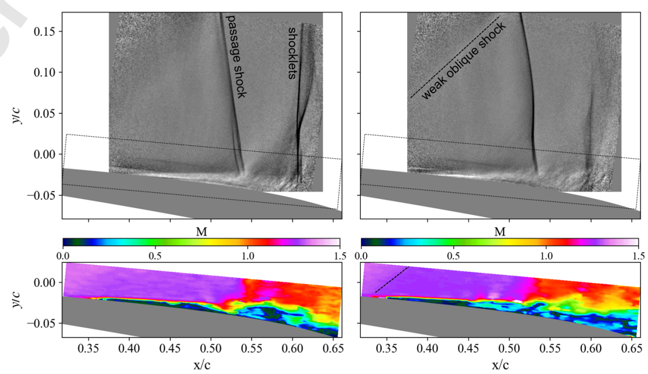

Fig. 14 Sequential snapshots, shadowgraph (Top) and TR-PIV (bottom), the dashed box indicates the FOV for TR-PIV. Time separation between left and right column is 0.3 ms (1.1 t_c) (color version online).

that oblique shock systems above the separation bubble occur mainly at higher frequencies compared to f_b, particularly pronounced at the tone and its first harmonics. Interestingly, such events with large separations are also visible in the TR shadowgraphs, as shown in the two consecutive samples in Fig. 14: when large separations occur, the higher blocking of which causes shocklets to occur above the separation. These shocklets migrate upstream as the laminar separation bubble grows in the vicinity of the main shock (Fig. 14, right). At about the same time, oblique shock waves occur in front of the passage shock which increase the incidence on the main shock and thus could be part of the feedback

Journal of Turbomachinery. Received September 18, 2024;
Accepted manuscript posted December 17, 2024. doi:10.1115/1.4067467

mechanism of self sustained oscillations at frequencies higher then f_b. Such an increase in the size of the laminar separation bubble can also be seen in Fig. 2 in the lower two frames. Also, following a wave propagation feedback mechanism by [1] one should expect upstream traveling pressure information that originates from the trailing edge and that periodically pushes the main shock toward upstream at f_b. In the following, the propagation of disturbances in the velocity field synchronized with the main shock motion is therefore investigated by cross-correlations of the time traces of velocity and shock position.

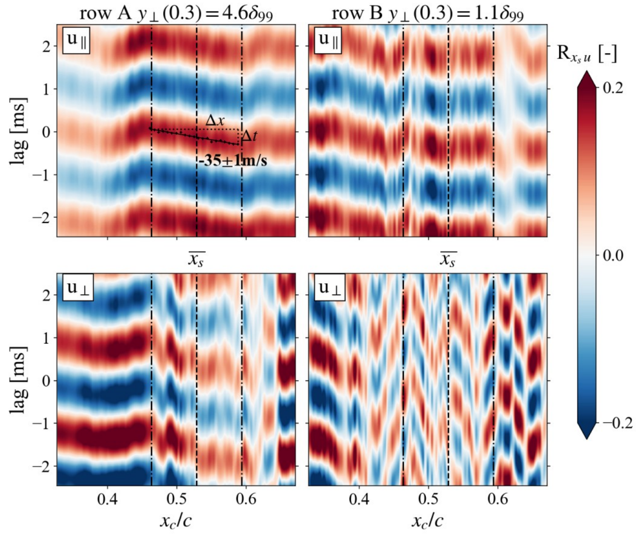

Fig. 15 Cross-Correlation map $x_s u$ for the low-band from TR-PIV in region *SBLI 2* along far-wall (left) and near-wall (right) particle image rows *A,B* as indicated in Fig. 5 (color version online).

Since the main shock is not always present in the small FOV for TR-PIV depending on the size of the separation, high density gradients in the time-synchronized shadow images were tracked by image processing instead, as described in [8,10].

Timetraces of the position of the main shock $x_s(t)$ are cross-correlated with $u_\perp, u_\parallel$ from near-wall and far-wall particle image rows *A, B* (cf. Fig. 5) to obtain wave propagation velocities of shock synchronous disturbances, similar to an analysis described for two-point-correlations by [18] and similar to evaluations in an earlier transonic cascade experiment [10,19]:

$$R_{x_s,u}(i\Delta t) = \frac{\sum_{i=-k}^{k} x_s'(t)\, u'(t + i\Delta t)}{\sigma_{x_s'}\, \sigma_{u'}}\,, \tag{3}$$

Here, k is the maximum lag, Δt is the time delay between successive frames, x_s' is the shock position and u' is the velocity, both centered by their mean value, and $\sigma_{x_s'}$, $\sigma_{u_s'}$ are the standard deviations. This approach was preferred over optional two-point correlations of velocity, as the latter were recorded in spatially separated regions and would therefore also require spatially separated reference points in each FOV, while taking the vibration of the main shock x_s provides a common reference. It is assumed that spatial tracking of the main shock excursions in the shadowgraphs is synonymous with tracking of large density gradients $x_s(t)$ in the flow.

Before cross-correlation of signals, $u_\parallel$, $u_\perp$ and x_s were centered with their mean and filtered forward-backward in the bands $0.5 \leq f \leq 0.6$ kHz (main buffet frequency), from $1.1 \leq f \leq 1.2$ kHz (the tone) and from $2.1 \leq f \leq 2.3$ kHz (first harmonic of the tone) using a digital 3rd-order Butterworth band pass. Cross-correlation maps were averaged over all 8 bursts of a run. Propagation velocities are obtained by a linear fit of local slopes in the fringes as indicated

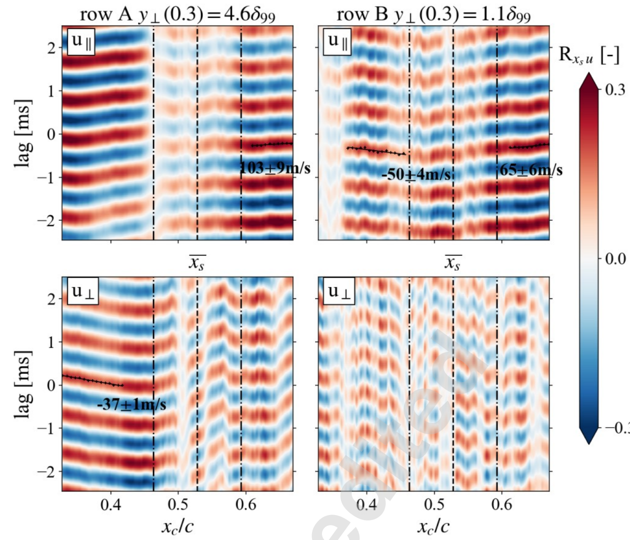

Fig. 16 Cross-Correlation map $x_s u$ in region *SBLI 2* at the tone at 1.1khz along far-wall (left) and near-wall (right) particle image rows *A,B* as indicated in Fig. 5 (color version online).

in Fig. 15 for which the standard error is provided. Since the TR PIV and shadowgraph recordings were acquired in non-overlapping temporal windows but with a fixed time lag, the correlation maps of repeat runs were compared and found to have consistent slopes in the fringe pattern but different offsets along the lag axis.

For region *SBLI 2* the cross-correlation maps in the low band indicate upstream propagation of disturbances for the far-wall row *A* within the min, max range of passage shock excursions Δ_{max} as indicated by dashed lines in Fig. 15. This essentially reflects the low-frequency shock motion and shows that, starting from the foremost shock position (indicated by the dashed dotted line) , the phase lag between $x_s'(t)$ and $u'(t)$ is decreasing with the chord-wise position.

Also, from Fig. 16 an upstream propagation of disturbances beyond the shock oscillation range Δ_{max} with higher propagation velocities than in the low band is evident. Although not shown here, similar results were obtained for the first harmonic of the tone.

Figure 17 confirms that this upstream movement of disturbances at high frequencies continues with lower propagation velocity in the region *Inflow*, beyond $x_c/c = 0.34$ (mean point of separation) to about $x_c/c = 0.25$, but only along the near-wall sampling line *B*. An upstream interaction up to this position is also confirmed in numerical results within space-time diagrams of pressure variations along the suction side which are described in the following parts of this series.

Although not shown here, similar cross-correlation maps from data obtained in the TE-PS area showed no indication for upstream propagation of disturbances from the wake at relevant frequencies. TR measurements near the trailing edge of blade no.3 were not aquired due to structural limitations at the TGK, so that shock-synchronous feedback from the TE-SS could not be verified.

5 Conclusions

Time-resolved PIV measurements are performed on the DLR transonic compressor cascade TCTA at an inlet Mach number up to 1.22. Using a state-of-the-art high-speed camera and a double pulse high-speed laser system with output power of 2×10 W a light-sheet heights of ~ 4 mm (6% of cascade pitch) was feasible at sampling rates near 20 kHz. Multiple time sequences (bursts) each with duration of $\sim 2000\, t_c$ could be recorded at three measurement stations in the center passage of the cascade at mid-span, while

Journal of Turbomachinery. Received September 18, 2024;
Accepted manuscript posted December 17, 2024. doi:10.1115/1.4067467

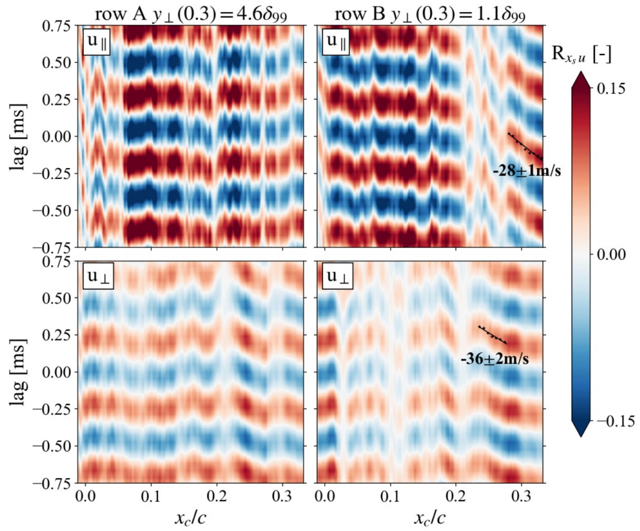

Fig. 17 Cross-Correlation map $x_s u$ in region *Inflow* for the first harmonic of the tone along far-wall (left) and near-wall (right) particle image rows *A,B* as indicated in Fig. 5 (color version online).

density variations of the SBLI were acquired with an additional camera synchronized with the PIV sample rate. Results indicate that mean 2d flow fields obtained with TR-PIV are consistent with the mean values and axial fluctuations of the large-scale PIV measurement data previously obtained from PIV measurements in the TCTA (see Fig. 4). Tracing of the main passage shock and Fourier analyzing the shock excursions in the shadowgraphs confirms the PSD distributions recently analyzed from HS schlieren [8] match well. A Fourier analysis along sampling rows in the TR-PIV data provides information on the 1d chord-wise spatial distribution of PSD of velocity also containing specific peaks (tones) and broad peaks also visible in the shock buffet spectrum. To find sources of distinct tones at the entrance of a passage, a SPOD is performed on high-speed schlieren recordings from an earlier measurement campaign, which covers the unsteady shock systems in three passages. Results indicate that tonal peaks can be associated to vibrations of bow and lip shocks in the lower two passages that oscillate in anti-phase. It was found that the main passage shock oscillates in-phase and in anti-phase at different peaks in the low frequency band of shock buffet. Inspection of spatio-temporal modes of velocity fluctuations at specific broad peaks and tones in the buffet frequency range indicate that upstream of the main shock oblique shock waves occur at higher order harmonics of the fundamental buffet frequency as well for specific high-frequency tones in the buffet spectrum. Timetraces of the main shock position x_s were cross-correlated with timetraces of axial and transverse velocities to obtain propagation velocities of disturbances at specific frequency ranges of shock excursions. The upstream propagation of disturbances beyond the excursion range of the main shock was observed for the dominant buffet frequency as well as for the high-frequency tone and its first harmonic. The upstream propagating of distortions at higher frequencies is consistent with the occurance of oblique shock waves that travel at higher speed than the main shock and are probably part of the feedback mechanism for self sustained shock oscillations in transonic cascade flows which is subject of part 2 and 3 of this paper series.

Acknowledgment

The authors would like to thank Jasmin Flamm for the excellent technical support in carrying out the experiments and Sebastian Grund for constructive improvements to the TGK for particle feeding.

Funding

This work was made possible through DLR-internal funding.

Conflict of Interest

There are no conflicts of interest.

Data Availability Statement

The datasets generated and supporting the findings of this article are obtainable from the corresponding author upon reasonable request.

Nomenclature

Acronyms

ADP = Aerodynamic Design Point
BL = Boundary layer
PSD = Power spectral density
CTU = convective time unit cu_1^-1
FOV = Field of view
HSS = High speed schlieren imaging
IRW = PIV interrogation window
LE,TE = Leading edge, Trailing edge
MP1 = Measurement plane at the cascade entry
PIV = Particle Image Velocimetry
POD = Proper Orthogonal Decomposition
rms = root mean square or standard deviation
SBLI = Shock Boundary layer Interaction
SPOD = Spectral POD
TCTA = Transonic Cascade TEAMAero
TR = Time-resolved
HR = High spatial Range
SC = Schlieren imaging

Roman letters

M = isentropic Mach number
m = Magnification [µm/pixel]
c = Blade chord length [mm]
f_s, f_b = Sampling frequency, dominat buffet frequency [kHz]
t_c = Convective time or CTU cu_1^-1 [ms]
Δt_p = PIV double pulse separation [µs]
H = Shape factor $\delta^* \theta^{*-1}$
u, v = Velocity components along x, y [m/s]
x_s = Shock position [mm]

Greek letters

δ_{99} = BL thickness at $0.99u_e$ [µm]
δ^* = Displacement thickness [µm]
θ^* = Momentum thickness [µm]
ν = Kinematic viscosity [m^2 s^{-1}]

Dimensionless values

Re = Reynolds number, $u_1 c \nu^{-1}$
Sr = Strouhal number, $f\, t_c$

Superscripts and subscripts

1 = Inlet value measured in MP1
$'$ = centered by the mean value
c = aligned with chord / compressible
e = Boundary-layer edge value
i = image coordinates
$\parallel$ = wall-parallel component
$\perp$ = wall-normal component

Journal of Turbomachinery. Received September 18, 2024;
Accepted manuscript posted December 17, 2024. doi:10.1115/1.4067467

References

[1] Lee, B., 2001, "Self-sustained shock oscillations on airfoils at transonic speeds," Progress in Aerospace Sciences, **37**(2), pp. 147 – 196.

[2] Crouch, J. D., Garbaruk, A., Magidov, D., and Travin, A., 2009, "Origin of transonic buffet on aerofoils," Journal of Fluid Mechanics, **628**, pp. 357–369.

[3] Klinner, J., Munoz Lopez, E. J., Hergt, A., and Willert, C., 2023, "High-resolution PIV measurements of the shock boundary layer interaction within a highly loaded transonic compressor cascade," *15th International Symposium on Particle Image Velocimetry – ISPIV 2023*, https://elib.dlr.de/197278/

[4] Towne, A., Schmidt, O. T., and Colonius, T., 2018, "Spectral proper orthogonal decomposition and its relationship to dynamic mode decomposition and resolvent analysis," Journal of Fluid Mechanics, **847**, pp. 821–867.

[5] Schmidt, O. T. and Colonius, T., 2020, "Guide to Spectral Proper Orthogonal Decomposition," AIAA Journal, **58**(3), pp. 1023–1033.

[6] Munoz Lopez, E. J., Hergt, A., Ockenfels, T., Grund, S., and Gümmer, V., 2023, "The Current Gap between Design Optimization and Experiments for Transonic Compressor Blades," International Journal of Turbomachinery, Propulsion and Power, **8**(4), p. 47.

[7] Munoz Lopez, E. J., Hergt, A., Grund, S., and Gümmer, V., 2023, "The New Chapter of Transonic Compressor Cascade Design at the DLR," Journal of Turbomachinery, **145**(81001).

[8] Munoz Lopez, E. J., Hergt, A., Klinner, J., Grund, S., Karboujian, J., Flamm, J., and Gümmer, V., 2023, "Investigations of the Unsteady Shock-Boundary Layer Interaction in a Transonic Compressor Cascade," *Turbo Expo: Power for Land, Sea, and Air*, doi: 10.1115/GT2023-102622.

[9] Giepman, R. H. M., Schrijer, F. F. J., and van Oudheusden, B. W., 2015, "High-resolution PIV measurements of a transitional shock wave–boundary layer interaction," Experiments in Fluids, **56**(6), p. 113.

[10] Klinner, J., Hergt, A., Grund, S., and Willert, C. E., 2021, "High-Speed PIV of shock boundary layer interactions in the transonic buffet flow of a compressor cascade," Experiments in Fluids, **62**(3), p. 58.

[11] Munoz Lopez, E. J., Klinner, J., Hergt, A., and Willert, C., 2024, "The unsteady Shock-Boundary Layer Interaction in a Compressor Cascade: Time resolved Measurements - Promotional Videos," doi: 10.5281/zenodo.14264703.

[12] Willert, C. E., Mitchell, D. M., and Soria, J., 2012, "An assessment of high-power light-emitting diodes for high frame rate schlieren imaging," Experiments in Fluids, **53**(2), pp. 413–421.

[13] Westerweel, J. and Scarano, F., 2005, "Universal outlier detection for PIV data," Experiments in Fluids, **39**(6), pp. 1096–1100.

[14] Schlichting, H. and Gersten, K., 2017, *Boundary-Layer Theory*, Springer Berlin Heidelberg, Berlin, Heidelberg.

[15] Burrows, T., 2020, "Spectral Proper Orthogonal Decomposition in Python," https://github.com/tjburrows/spod_python

[16] Cottier, S., Combs, C. S., and Vanstone, L., 2019, "Spectral Proper Orthogonal Decomposition Analysis of Shock-Wave/Boundary-Layer Interactions," *AIAA Aviation 2019 Forum*, American Institute of Aeronautics and Astronautics, doi: 10.2514/6.2019-3331.

[17] Hoffman, E. N. A., Rodriguez, J. M., Cottier, S. M., Combs, C. S., Bathel, B. F., Weisberger, J. M., Jones, S. B., Schmisseur, J. D., and Kreth, P. A., 2023, "Modal Analysis of Cylinder-Induced Transitional Shock-Wave/Boundary-Layer Interaction Unsteadiness," AIAA Journal, **60**(5), pp. 2730–2748.

[18] Hartmann, A., Klaas, M., and Schröder, W., 2012, "Time-resolved stereo PIV measurements of shock–boundary layer interaction on a supercritical airfoil," Experiments in Fluids, **52**(3), pp. 591–604.

[19] Hergt, A., Klinner, J., Willert, C., Grund, S., and Steinert, W., 2022, "Insights into the Unsteady Shock Boundary Layer Interaction," *Turbo Expo: Power for Land, Sea, and Air*, American Society of Mechanical Engineers: New York, NY, USA, Rotterdam, doi: 10.1115/GT2022-82720.

[20] Klose, B. F., Morsbach, C., Bergmann, M., Hergt, A., Klinner, J., Grund, S., and Kuegeler, E., 2023, "A Numerical Test Rig for Turbomachinery Flows Based on Large Eddy Simulations With a High-Order Discontinuous Galerkin Scheme - Part 2: Shock-Capturing and Transonic Flows," Journal of Turbomachinery, **146**(2), pp. 1–12.

[21] Giannelis, F., N., Vio, A., G., and Levinski, O., 2017, "A review of recent developments in the understanding of transonic shock buffet," Progress in Aerospace Sciences, **92**, pp. 39 – 84.

[22] He, X., Fang, Z., Rigas, G., and Vahdati, M., 2021, "Spectral proper orthogonal decomposition of compressor tip leakage flow," Physics of Fluids, **33**(10), p. 105105.

Journal of Turbomachinery. Received September 18, 2024;
Accepted manuscript posted December 17, 2024. doi:10.1115/1.4067467

List of Figures

List of Tables